Shock-particle-interaction study with a hyperbolic two-fluid model

Victor Boniou, Rodney O. Fox

Shock–particle-interaction study with a hyperbolic two-fluid model

Victor Boniou[a], Rodney O. Fox[a,b]

[a]*Department of Chemical and Biological Engineering, Iowa State University, Ames, IA 50011-1098, USA*
[b]*Laboratoire EM2C, CNRS, CentraleSupélec, Université Paris-Saclay, 3 rue Joliot-Curie, 91192 Gif-sur-Yvette, France*

Abstract

A hyperbolic two-fluid model for high-speed, monodisperse, gas–particle flow is employed to study the interaction of a thin, moderately dense (volume fraction $\alpha_p < 0.2$) particle curtain impacted by an incident shock with Mach number $\mathcal{M}_s$. Mimicking the experimental setup, the numerical setup consists of a one-dimensional shock tube with a thin particle curtain in the driven section. This allows to validate the two-fluid model against recent experimental campaigns exploring a wide range of particle diameters, material densities, volume fractions, curtain widths and shock speeds. In general, the two-fluid model allows to reproduce the experimental data where the highest discrepancy is obtained in the configurations with the smallest $\mathcal{M}_s$. However, the main goal of this study is to explore the closures used in the two-fluid model. Attention is drawn to the particle-Mach-number ($\mathcal{M}_p$) dependence of the drag and added-mass coefficients, which have not yet been explored extensively in the literature. Also, the two-fluid model based on kinetic theory includes a particle pressure accounting for particle–fluid–particle (pfp) interactions. Thus, a parametric study is presented to evaluate the impact of several model parameters such as the drag coefficient, the added-mass coefficient, and the magnitude of the pfp pressure. The complete drag model accounting for particle Reynolds number Re_p, $\mathcal{M}_p$ and α_p is more accurate than previous drag models depending only on Re_p and α_p. Due the high particle-to-gas density ratio, the added-mass model has only a minor impact on the results. On the other hand, the magnitude of the pfp pressure has a real impact on the spread of the curtain due to the high slip velocity.

Keywords: gas–particle flow, kinetic theory of granular flow, added mass, pseudoturbulence, shock-particle interactions

1. Introduction

The study of a shock interacting with particles has a long history starting from late 1980s with the pioneering theoretical work of Forney et al. [8]. The main difficulty when dealing with compressible flows is the large range of space and time scales. This feature of high–speed, gas–particle flows make them challenging to study for both experimental and numerical approaches. On top of that, the high volume fraction (> 0.1) and shock Mach number (> 0.6) also imply four-way coupling [4] between gas and particles. Indeed, when particles are close to each other, they have an impact on the gas, but also on neighboring particles through collisions and friction. Some recent direct-numerical simulations (DNS) have demonstrated that the flow-field fluctuations (or pseudoturbulence) [14, 22, 25] are not negligible in random arrays of spheres interacting with planar shocks. Furthermore, the contribution of unsteady forces such as added mass [17] and Basset history [9] can become predominant in the early moments when the shock enters in a dense particle zone.

Numerous studies, both experimental and numerical, have been carried out to yield more insight into the physics behind this problem. While some researchers focused on the study of the microscale where an isolated particle is passed by a high-speed flow, the importance of four-way coupling was the motivation to develop macroscale approaches where the entire granular phase is considered. While the former provides a better understanding of the force balance, the latter paves the way to accurate modeling of complex gas–particle systems [15]. Indeed, the numerous

Email addresses: boniouv@iastate.edu (Victor Boniou), rofox@iastate.edu (Rodney O. Fox)

numerical studies resulted in the assessment of more complete model for drag, which also takes into account the particle-Mach-number dependency [4, 20].

For the macroscale description, the pioneering work of Rogue et al. [30] proposed a first experimental setup to study the interaction of a shock with a particle curtain. The investigation is also accompanied by a numerical study making use of a two-fluid compressible model [31]. Later, a shock tube has been dedicated to the study of multiphase flows at the Sandia National Laboratory (SNL) [37] with a focus on moderately dense granular flows interacting with a shock wave. Finally, the ASOS shock tube has also been adapted to the study of thicker curtains in a wider range of flow conditions from subsonic to supersonic regimes [35]. While the pioneer experiments on the subject were based on a vertical shock tube with particles contained in a diaphragm, the ASOS and SNL experimental setups consist of an horizontal shock tube with a gravity-fed particle curtain. This curtain generation technique allows to explore the dense gas–solid regime with a volume fraction comprised between 1 to 50 %.

While many of the flow solvers used in the literature to simulate a high-speed gas with particles rely on Eulerian–Lagrangian methods, our proposed framework employs an Eulerian representation of the particle phase. Euler–Euler (EE) methods can rely either on the Baer—Nunziato equations [1] or on the kinetic theory of granular flow for the particle phase [12]. The resulting solvers [15, 28, 30, 32] are then able to model dilute-to-dense granular multiphase flows. In the literature, experimental studies have been mainly focused on the development of universal scaling laws to predict the curtain spreading rate [6, 7, 35], while in numerical works, the use of the shock-curtain case was used among other validation test cases to assess the numerical methods more than the modeling [15, 28, 32]. However, more extensive studies have been performed to propose model improvements based on a comparison of experimental and numerical results for monodisperse [18, 30] and bidisperse granular phase [40]. This work proposes to follow the same path to assess and improve the modeling of high-speed, monodisperse, gas–particle flows. Our model is based on an EE formulation derived from kinetic theory [3], which has the advantage to naturally handle hyperbolicity issues. The model also includes pseudo-turbulent kinetic energy (PTKE) of the gas phase to account for the two-way coupling, and internal energy of the particle phase to model heat transfer between the gas and particles.

This work starts with the presentation of the two-fluid model in section 2. In section 3, the closures for drag, added mass and particle–fluid–particle (pfp) pressure are further discussed, especially with their dependency on the particle Mach number. Then, the numerical setup used to replicate the experimental particle-curtain configurations is presented in section 4. Results are presented in section 5 where twelve configurations are explored and compared to recent experimental data with various drag, added-mass and pfp-pressure models. Finally, conclusions are drawn in section 6.

2. Governing equations

This section focuses on the governing equations for gas–particles flows based on the two-fluid model from [3]. The added-mass contribution is naturally accounted for and the equation system does not suffer from ill-posedness encountered by the conventional compressible two-fluid models containing two-way coupling (Archimedes forces) [16]. The flow-field fluctuations are also modeled through the transport of PTKE of the gas k_g. Finally, the model includes the transport of internal energy of particles e_p to properly predict the inter-phase heat transfer, which plays a significant role of weakening shocks in the dense granular regime [15]. By transporting k_g and e_p, the complete energy cascade is modeled. Heating of the particles due to inelastic collisions acts as a source term for e_p.

In our EE formulation, the gas material density is denoted by ρ_g, and the solids material density ρ_p is constant. The gas- and particle-phase velocities are $\mathbf{u}_g$ and $\mathbf{u}_p$, respectively. The total energies of the fluid and particle phases are denoted as E_g and E_p, respectively. The total energy is made up of the kinetic + internal energies. We denote the former for each phase as K_f and K_p, and the latter as e_f and e_p, respectively. Hence, $E_g = K_g + e_g$ and $E_p = K_p + e_p$. The kinetic energy is further divided into mean and fluctuating components: $K_g = \frac{1}{2}u_g^2 + k_g$ and $K_p = \frac{1}{2}u_p^2 + \frac{3}{2}\Theta_p$. Here, $u^2 = \mathbf{u} \cdot \mathbf{u}$ and Θ_p is the granular temperature. PTKE represents fluid-velocity fluctuations due to finite-size particles, and the square root of Θ_p represents the velocity magnitude of individual particles relative to $\mathbf{u}_p$. In the two-fluid model, the total energy of both phases is conserved. While the gas phase directly derives from the Euler equations, it is convenient to solve transport equations for E_g and k_g and to deduce e_g. In contrast, for the particle phase, the kinetic theory description leads naturally to transport equations for K_p and e_p, and we then compute Θ_p from them. The thermodynamic temperatures T_g and T_p (K) are found from the internal energies e_g and e_p, respectively.

2.1. Treatment of added mass

While added mass is often modeled by an additional inter-phase force term leading to the so-called virtual-mass force [5], our EE model directly handles added mass by assigning a fraction of the gas phase surrounding a particle to move with the velocity of the particle phase $\mathbf{u}_p$. The volume fraction of reference for the particle phase in the two-fluid model is then replaced by $\alpha_p^\star = \alpha_p + \alpha_a$ where α_a is the volume fraction of the added-mass phase, while α_p is the particle-phase volume fraction. The gas counterpart is then $\alpha_g^\star = \alpha_g - \alpha_a$ where α_g is the gas-phase volume fraction. The mass balances (constant ρ_p, no mass transfer from solid to gas) for the particle and added-mass phases are, respectively,

$$\partial_t \alpha_p + \partial_{\mathbf{x}} \cdot \alpha_p \mathbf{u}_p = 0 \tag{1}$$

and

$$\partial_t \rho_g \alpha_a + \partial_{\mathbf{x}} \cdot \rho_g \alpha_a \mathbf{u}_p = S_a \tag{2}$$

where S_a is a mass-transfer rate from the continuous gas phase to the added-mass phase, which is detailed in section 3.2. This source term also leads to momentum and energy exchanges between the added-mass phase and the continuous gas phase defined by

$$\mathbf{S}_{gp} = \max(S_a, 0)\, \mathbf{u}_g + \min(S_a, 0)\, \mathbf{u}_p \tag{3}$$

and for the total energy by

$$S_E = \max(S_a, 0)\, E_g + \min(S_a, 0)\, E_p. \tag{4}$$

In words, if S_a is positive, gas-phase mass, momentum and total energy are transferred from the continuous phase to the added-mass phase, while for negative S_a the transfer is in the opposite direction. Note that in the following, S_E is further divided into an internal-energy source S_e and a kinetic-energy source S_K defined in the same manner as eq. (3) and eq. (4).

In summary, the inclusion of added mass requires an additional continuity equation defined by eq. (2), along with source terms to model changes in the added-mass volume fraction, momentum and total energy. The total mass of the particle + added-mass phase can be expressed as

$$\rho_e \alpha_p^\star = \rho_p \alpha_p + \rho_g \alpha_a, \tag{5}$$

which defines the effective density ρ_e. In the next section, we present a two-fluid model for monodisperse particles with added mass and internal energy. This model has balance equations for the particle-phase variables $\rho_e \alpha_p^\star$, $\rho_e \alpha_p^\star \mathbf{u}_p$, $\rho_e \alpha_p^\star K_p$, and $\rho_e \alpha_p^\star e_p$. In addition, the conserved variable $\rho_p \alpha_p$, governed by eq. (1), is needed to determine ρ_g when the fluid is compressible.

Note that given α_p and the two conserved variables for the phase masses ($\rho_g \alpha_g^\star$, $\rho_e \alpha_p^\star$), the added-mass volume fraction α_a is found from

$$\alpha_a = \frac{\kappa}{1+\kappa}(1-\alpha_p) \qquad \text{for} \qquad \kappa = \frac{\rho_e \alpha_p^\star - \rho_p \alpha_p}{\rho_g \alpha_g^\star} = \frac{\alpha_a}{\alpha_g^\star} \tag{6}$$

with $\alpha_g = 1 - \alpha_p$, and then $\alpha_p^\star = \alpha_p + \alpha_a$ and $\alpha_g^\star = \alpha_g - \alpha_a$. Thus, for constant ρ_p, the primitive variables (α_p, ρ_e, ρ_g, $\mathbf{u}_p$, $\mathbf{u}_g$, K_p, e_p, E_g, k_g) are uniquely defined from the conserved variables ($\rho_p \alpha_p$, $\rho_e \alpha_p^\star$, $\rho_g \alpha_g^\star$, $\rho_e \alpha_p^\star \mathbf{u}_p$, $\rho_g \alpha_g^\star \mathbf{u}_g$, $\rho_e \alpha_p^\star K_p$, $\rho_e \alpha_p^\star e_p$, $\rho_g \alpha_g^\star E_g$, $\rho_g \alpha_g^\star k_g$).

2.2. Transport equations for the particle phase

The kinetic model described in [3] yields transport equations for mass, momentum, kinetic energy and internal energy of the phase comprising particles and added mass:

$$\partial_t \rho_e \alpha_p^\star + \partial_{\mathbf{x}} \cdot \rho_e \alpha_p^\star \mathbf{u}_p = S_a \tag{7}$$

$$\partial_t \rho_e \alpha_p^\star \mathbf{u}_p + \partial_{\mathbf{x}} \cdot [\rho_e \alpha_p^\star (\mathbf{u}_p \otimes \mathbf{u}_p + \Theta_p \mathbf{I} + P_p \mathbf{I}) + \mathbf{P}_{pfp}] = -\mathbf{D} - \alpha_p^\star (\partial_{\mathbf{x}} \hat{p}_g + \mathbf{F}_{pg}) + \mathbf{S}_{gp} \tag{8}$$

$$\partial_t \rho_e \alpha_p^\star K_p + \partial_{\mathbf{x}} \cdot [\rho_e \alpha_p^\star \mathbf{u}_p (K_p + \Theta_p + P_p) + \mathbf{P}_{pfp} \cdot \mathbf{u}_p] = \mathbf{P}_{pfp} : \partial_{\mathbf{x}} \mathbf{u}_p - D_E - \alpha_p^\star \mathbf{u}_p \cdot (\partial_{\mathbf{x}} \hat{p}_g + \mathbf{F}_{pg}) - H_p + S_K \tag{9}$$

$$\partial_t \rho_e \alpha_p^\star e_p + \partial_{\mathbf{x}} \cdot \rho_e \alpha_p^\star \mathbf{u}_p e_p = -H_{pg} + H_p + S_e \tag{10}$$

where $\mathbf{P}_{pfp} : \partial_{\mathbf{x}}\mathbf{u}_p$ is the work done by the pfp pressure on the particles to reduce their volume fraction.[1] The particle-phase pressure $P_p = P_c + P_f$ consists of two contributions. A collisional component:

$$P_c = 2(1 + e_c)\alpha_p g_0 \Theta_p, \quad g_0 = \frac{1 + \alpha_g}{2\alpha_g^3} \tag{11}$$

where e_c is the coefficient of restitution, and a frictional component:

$$P_f = \frac{p_f \alpha_p g_0}{\rho_e \alpha_p^\star} \frac{1}{2}\left[1 + \tanh\left(\frac{\alpha_p - \alpha_{max}}{\Delta_f}\right)\right] \tag{12}$$

where $\alpha_{max} = 0.63$ is the close-packed limit and Δ_f controls the sharpness of the pressure transition at α_{max}. For the particle curtains investigated in this work ($\alpha_p < 0.20$), neither component of P_p has a significant influence on the spreading rate.

The pfp pressure tensor described in [11] is modeled as

$$\mathbf{P}_{pfp} = C_{pfp}\rho_g \alpha_p^\star \mathbf{R}. \tag{13}$$

The slip-pressure tensor $\mathbf{R}$ for potential flow around spheres is derived from kinetic theory [10] as

$$\mathbf{R} = \frac{1}{5}u_{pg}^2 \mathbf{I} + \frac{2}{5}\mathbf{u}_{pg} \otimes \mathbf{u}_{pg} \tag{14}$$

where $\mathbf{u}_{pg} = \mathbf{u}_p - \mathbf{u}_g$ is the slip velocity. Notice that the trace of $\mathbf{R}$ is equal to u_{pg}^2 such that the trace of $\mathbf{P}_{pfp}$ (used in the 1-D model) is $C_{pfp}\rho_g \alpha_p^\star u_{pg}^2 \geq 0$. In general, the trace of $\mathbf{R}$ is always u_{pg}^2, but the coefficient of the isotropic part in eq. (14) need not be 1/5 [39]. The modeling of C_{pfp} is discussed in section 3.3 and investigated in section 5.

The momentum-exchange term $\mathbf{F}_{pg}$ is defined as

$$\mathbf{F}_{pg} = \mathbf{R} \cdot \partial_{\mathbf{x}}\rho_g - \frac{2}{3}\rho_g tr(\mathbf{\Gamma})\,\mathbf{u}_{pg} - \frac{4}{5}\rho_g \mathbf{S} \cdot \mathbf{u}_{pg} \tag{15}$$

where the gas-phase deformation rate tensor is $\mathbf{\Gamma} = \frac{1}{2}\left[\partial_{\mathbf{x}}\mathbf{u}_g + (\partial_{\mathbf{x}}\mathbf{u}_g)^t\right]$ and $\mathbf{S} = \mathbf{\Gamma} - \frac{1}{3}tr(\mathbf{\Gamma})\mathbf{I}$. The modeling of the added-mass source term S_a is discussed in section 3.2 while the corresponding momentum and energy source terms were defined by eq. (3) and eq. (4).

The drag-exchange terms for momentum and total energy are defined by

$$\mathbf{D} = \frac{\rho_e \alpha_p^\star}{\tau_p}\mathbf{u}_{pg}, \quad D_E = \frac{\rho_e \alpha_p^\star}{\tau_p}[\mathbf{u}_p \cdot \mathbf{u}_{pg} + 3a\Theta_p - 2(1 - a)k_g] \tag{16}$$

with τ_p the drag time scale discussed in section 3.1. The parameter a depends on the material densities:

$$a = \frac{\rho_p + \rho_g a_{min}}{\rho_p + \rho_g} \tag{17}$$

where $a_{min} = 0.5$ determines the steady-state ratio Θ_p/k_g for gas bubbles in a liquid (i.e., $\rho_p \ll \rho_g$). For the gas–particle flows investigated in this work, $\rho_p \gg \rho_g$ so that $a \lessapprox 1$. The Gunn correlation [13] for the Nusselt number (Nu, see table 2) given in [15] is used to model the inter-phase heat transfer:

$$H_{pg} = \frac{6\alpha_p^\star \lambda_g Nu}{d_p^2}(T_p - T_g) \tag{18}$$

where the phase temperatures are found from their internal energies: $T_g = \gamma_g e_g / C_{p,f}$, $T_p = e_p / C_{V,p}$. The particle

[1] According to the mass balance $D_t\alpha_p = \partial_t\alpha_p + \mathbf{u}_p \cdot \partial_{\mathbf{x}}\alpha_p = -\alpha_p \partial_{\mathbf{x}} \cdot \mathbf{u}_p$, when $\partial_{\mathbf{x}} \cdot \mathbf{u}_p > 0$ the value of α_p following the Lagrangian trajectory with velocity $\mathbf{u}_p$ will decrease.

diameter is d_p and λ_g is the fluid-phase thermal conductivity.

Finally, the particle-phase heating rate H_p is the sum of two contributions: a collisional contribution $\langle eC \rangle$ and a frictional contribution $\langle eF \rangle$. The collisional source term is modeled using the inelastic BGK closure [2, 27]

$$\langle eC \rangle = \rho_e \alpha_p^\star \frac{(1 - e_c^2)}{\tau_c} \Theta_p. \tag{19}$$

with e_c the coefficient of restitution and τ_c the collision time that depends on α_p and Θ_p:

$$\tau_c = \frac{d_p \sqrt{\pi}}{12 \alpha_p g_0 \Theta_p^{1/2}}. \tag{20}$$

The frictional contribution to the particle-phase heating term is

$$\langle eF \rangle = \rho_e \alpha_p^\star \frac{1}{\tau_f} \Theta_p. \tag{21}$$

where τ_f is a time scale that depends on τ_c and $\partial_{\mathbf{x}} \cdot \mathbf{u}_p$:

$$\tau_f = \frac{2 c_f}{\max(|\partial_{\mathbf{x}} \cdot \mathbf{u}_p|, 1/\tau_c)} \left[1 + \tanh\left(\frac{\alpha_p - \alpha_{max}}{\Delta_f} \right) \right]^{-1}. \tag{22}$$

Here, $c_f = 0.01$ controls the frictional time scale above close packing. For the particle curtains investigated in this work, H_p has a negligible effect on the spreading rate.

2.3. Continuous gas-phase balance equations

In conservative form, the gas phase (excluding the added mass) is governed by mass, momentum, total-energy, and PTKE balances [3, 11]:

$$\partial_t \rho_g \alpha_g^\star + \partial_{\mathbf{x}} \cdot \rho_g \alpha_g^\star \mathbf{u}_g = -S_a \tag{23}$$

$$\partial_t \rho_g \alpha_g^\star \mathbf{u}_g + \partial_{\mathbf{x}} \cdot (\rho_g \alpha_g^\star \mathbf{u}_g \otimes \mathbf{u}_g + \hat{p}_g \mathbf{I}) = \mathbf{D} + \alpha_p^\star (\partial_{\mathbf{x}} \hat{p}_g + \mathbf{F}_{pg}) - \mathbf{S}_{gp} \tag{24}$$

$$\partial_t \rho_g \alpha_g^\star E_g + \partial_{\mathbf{x}} \cdot [\rho_g \alpha_g^\star \mathbf{u}_g E_g + (\alpha_g^\star \mathbf{u}_g + \alpha_p^\star \mathbf{u}_p) \hat{p}_g] = -\mathbf{P}_{pfp} : \partial_{\mathbf{x}} \mathbf{u}_p + D_E + \alpha_p^\star \mathbf{u}_p \cdot (\partial_{\mathbf{x}} \hat{p}_g + \mathbf{F}_{pg}) + H_{pg} - S_E \tag{25}$$

$$\partial_t \rho_g \alpha_g^\star k_g + \partial_{\mathbf{x}} \cdot \rho_g \alpha_g^\star \mathbf{u}_g k_g + \frac{2}{3} \rho_g \alpha_g^\star k_g \partial_{\mathbf{x}} \cdot \mathbf{u}_g = D_{PT} - \rho_e \alpha_p^\star \frac{C_g}{\tau_p} k_g \tag{26}$$

where $\hat{p}_g = p_g + \frac{2}{3} \rho_g k_g$ is the modified gas pressure. The gas pressure is found from the ideal-gas law:

$$p_g = (\gamma_g - 1) \rho_g \left(E_g - K_g \right) = (\gamma_g - 1) \rho_g e_g \tag{27}$$

where γ_g is the heat-capacity ratio. In the total energy balance, H_{pg} represents convective heat transfer from the particle phase due to the temperature difference [15]. The final terms on the right-hand sides of eq. (23)–eq. (25) represent exchanges between the continuous gas phase and the added-mass phase.

In the PTKE balance in eq. (26), D_{PT} represents drag exchange of PTKE with the particle phase:

$$D_{PT} = \frac{\rho_e \alpha_p^\star}{\tau_p} [u_{pg}^2 + 3a\Theta_p - 2(1 - a) k_g]. \tag{28}$$

The parameter C_g controls the rate of dissipation of PTKE into internal energy in the gas phase [33]. Here, we will use the correlation from PR-DNS with frozen particles [21]:

$$C_g^{-1} = \alpha_p [1 + 1.25 \alpha_g^3 \exp(-\alpha_p \alpha_g^{1/2} Re_p^{1/2})], \tag{29}$$

Table 1: Nine-equation, two-fluid model for 1-D shock–particle-curtain interactions. The P_{pfp} term is written here as a force in the momentum balances, but could also be written as a particle-phase pressure flux. In either case, P_{pfp} does not act as a source term for Θ_p.

Mass balances:

$$\partial_t \rho_g \alpha_g^\star + \partial_x \rho_g \alpha_g^\star u_g = -S_a$$
$$\partial_t \rho_e \alpha_p^\star + \partial_x \rho_e \alpha_p^\star u_p = S_a$$
$$\partial_t \alpha_p + \partial_x \alpha_p u_p = 0$$

Momentum balances:

$$\partial_t \rho_g \alpha_g^\star u_g + \partial_x (\rho_g \alpha_g^\star u_g^2 + \hat{p}_g) = \frac{\rho_e \alpha_p^\star}{\tau_p} u_{pg} + \alpha_p^\star (\partial_x \hat{p}_g + F_{pg}) - S_{fp}$$
$$\partial_t \rho_e \alpha_p^\star u_p + \partial_x [\rho_e \alpha_p^\star (u_p^2 + \Theta_p + P_p) + P_{pfp}] = -\frac{\rho_e \alpha_p^\star}{\tau_p} u_{pg} - \alpha_p^\star (\partial_x \hat{p}_g + F_{pg}) + S_{fp}$$

Gas-phase energy balances (total + PTKE):

$$\partial_t \rho_g \alpha_g^\star E_g + \partial_x [\rho_g \alpha_g^\star u_g E_g + (\alpha_g^\star u_g + \alpha_p^\star u_p)\hat{p}_g] = -P_{pfp} \partial_x u_p + \frac{\rho_e \alpha_p^\star}{\tau_p} [3a\Theta_p - 2(1-a)k_g + u_{pg} u_p]$$
$$+ \alpha_p^\star u_p (\partial_x \hat{p}_g + F_{pg}) + H_{pg} - S_E$$
$$\partial_t \rho_g \alpha_g^\star k_g + \partial_x \rho_g \alpha_g^\star u_g k_g + \frac{2}{3} \rho_g \alpha_g^\star k_g \partial_x u_g = \frac{\rho_e \alpha_p^\star}{\tau_p} [3a\Theta_p - 2(1-a)k_g + u_{pg}^2 - C_g k_g]$$

Particle-phase energy balances (kinetic + internal):

$$\partial_t \rho_e \alpha_p^\star K_p + \partial_x [\rho_e \alpha_p^\star u_p (K_p + \Theta_p + P_p) + u_p P_{pfp}] = P_{pfp} \partial_x u_p - \frac{\rho_e \alpha_p^\star}{\tau_p} [3a\Theta_p - 2(1-a)k_g + u_{pg} u_p]$$
$$- \alpha_p^\star u_p (\partial_x \hat{p}_g + F_{pg}) - H_p + S_K$$
$$\partial_t \rho_e \alpha_p^\star e_p + \partial_x \rho_e \alpha_p^\star u_p e_p = H_p - H_{pg} + S_e$$

where the particle Reynolds number is

$$Re_p = \frac{\rho_g d_p v_{pg}}{\mu_g} = \frac{\alpha_g^\star \rho_g d_p u_{pg}}{\alpha_g \mu_g}, \tag{30}$$

and μ_g is the gas-phase viscosity (which depends on T_g). The particle Mach number associated with the slip velocity is

$$\mathcal{M}_p = \frac{v_{pg}}{c_g} = \frac{\alpha_g^\star u_{pg}}{\alpha_g c_g} \tag{31}$$

with c_g is the gas speed of sound. In standard two-fluid models, Re_p and $\mathcal{M}_p$ are usually computed from the slip velocity $v_{pg} = (\mathbf{v}_{pg} \cdot \mathbf{v}_{pg})^{1/2}$, which is defined in the absence of added mass. As shown in [11], the slip velocities are related by $\alpha_g \mathbf{v}_{pg} = \alpha_g^\star \mathbf{u}_{pg}$, which modifies the definitions of Re_p and $\mathcal{M}_p$. In our formulation, the slip velocity with added mass is larger than without because part of the fluid moves with the particle velocity $\mathbf{u}_p$.

2.4. Final form of the 1-D nine-equation system for shock–particle-curtain interactions

Now that all the transport equations have been introduced, the 1-D two-fluid model for shock–particle-curtain interactions is summarized in table 1 and table 2 with additional parameters described in section 3.

Table 2: Summary of the terms appearing in the two-fluid model for 1-D shock–particle-curtain interactions in table 1. Different models for C_D, $c_m^\star$ and C_{pfp} are investigated in section 5.

$$\kappa = \frac{\rho_e \alpha_p^\star - \rho_p \alpha_p}{\rho_g \alpha_g^\star} \qquad \alpha_g = 1 - \alpha_p \qquad \alpha_a = \frac{\kappa}{1+\kappa}\alpha_g \qquad \alpha_p^\star = \alpha_p + \alpha_a \qquad \alpha_g^\star = \alpha_g - \alpha_a \qquad u_{pg} = u_p - u_f$$

$$S_a = \frac{\rho_g}{\tau_a}(c_m^\star \alpha_g \alpha_p - \alpha_a) \qquad S_{fp} = \max(S_a, 0)\, u_g + \min(S_a, 0)\, u_p \qquad S_E = \max(S_a, 0)\, E_g + \min(S_a, 0)\, E_p$$

$$S_K = \max(S_a, 0)\, K_g + \min(S_a, 0)\, K_p \qquad S_e = \max(S_a, 0)\, e_g + \min(S_a, 0)\, e_p$$

$$Re_p = \frac{\alpha_g^\star}{\alpha_g}\frac{d_p u_{pg}}{\nu_g} \qquad \mathcal{M}_p = \frac{\alpha_g^\star}{\alpha_g}\frac{u_{pg}}{c_g} \qquad \tau_a = C_a \tau_p \qquad \tau_p = \frac{4}{3}\frac{\rho_e}{\rho_g}\frac{d_p^2}{\nu_g C_D Re_p} \qquad H_{pg} = \frac{6\alpha_p^\star \lambda_g Nu}{d_p^2}(T_p - T_g)$$

$$Pr_g = \frac{\rho_g C_{p,f} \nu_g}{\lambda_g} \qquad Nu = (7 - 10\alpha_g + 5\alpha_g^2)(1 + 0.7 Re_p^{0.2} Pr_g^{1/3}) + (1.33 - 2.4\alpha_g + 1.2\alpha_g^2) Re_p^{0.7} Pr_g^{1/3}$$

$$p_g = (\gamma_g - 1)\rho_g e_g \qquad e_g = E_g - \frac{1}{2}u_g^2 - k_g \qquad \hat{p}_g = p_g + \frac{2}{3}\rho_g k_g \qquad T_g = \frac{\gamma_g e_g}{C_{p,g}} \qquad T_p = \frac{e_p}{C_{V,p}}$$

$$\tau_c = \frac{d_p\sqrt{\pi}}{12\alpha_p g_0 \Theta_p^{1/2}} \qquad \tau_f = \frac{2c_f}{\max(|\partial_x u_p|, 1/\tau_c)}\left[1 + \tanh\left(\frac{\alpha_p - \alpha_{max}}{\Delta_f}\right)\right]^{-1} \qquad H_p = \rho_e \alpha_p^\star \left[\frac{1}{\tau_c}(1 - e_c^2) + \frac{1}{\tau_f}\right]\Theta_p$$

$$\Theta_p = \frac{2}{3}K_p - \frac{1}{3}u_p^2 \qquad P_p = P_c + P_g \qquad P_c = 2(1 + e_c)\alpha_p g_0 \Theta_p \qquad P_f = \frac{p_f \alpha_p g_0}{2\rho_e \alpha_p^\star}\left[1 + \tanh\left(\frac{\alpha_p - \alpha_{max}}{\Delta_f}\right)\right]$$

$$C_g^{-1} = \alpha_p[1 + 1.25\alpha_g^3 \exp(-\alpha_p \alpha_g^{1/2} Re_p^{1/2})] \qquad a = \frac{\rho_p + \rho_g a_{min}}{\rho_p + \rho_g} \qquad g_0 = \frac{1 + \alpha_g}{2\alpha_g^3}$$

$$P_{pfp} = C_{pfp}\rho_g \alpha_p^\star u_{pg}^2 \qquad F_{pg} = u_{pg}^2 \partial_x \rho_g - (\gamma_g - 1)\rho_g(\partial_x u_g) u_{pg}$$

3. Closures for inter-phase exchanges

In the nine-equation system described in section 2, the closures for drag, added mass and pfp pressure have yet to be described. The aim of this section is to present different models from the literature with several levels of complexity. These closures will then be compared in section 5 to study the effect of these choices on the dynamics of a shock wave interacting with a thin particle curtain.

3.1. Drag model

In the absence of added mass, the drag time scale is found from

$$\frac{1}{\tau_p} = \frac{3}{4}\frac{1}{\rho_p} C_D Re_p \frac{\mu_g}{d_p^2} \tag{32}$$

where d_p is the particle diameter and C_D is a drag coefficient. In the Stokes limit where $C_D Re_p = 24$, eq. (32) yields the Stokes drag law. In order to account for added mass, we replace ρ_p with ρ_e in eq. (32):

$$\frac{1}{\tau_p} = \frac{3}{4}\frac{1}{\rho_e} C_D Re_p \frac{\mu_g}{d_p^2}, \tag{33}$$

and use the particle Reynolds number defined in eq. (30) to find C_D as described next. The momentum exchange term for fluid drag is thus

$$\mathbf{D} = -\frac{\rho_e \alpha_p^\star}{\tau_p}\mathbf{u}_{pg} = -\alpha_p^\star \frac{3}{4} C_D Re_p \frac{\mu_g}{d_p^2}\mathbf{u}_{pg}. \tag{34}$$

As shown in [11], this result is consistent with the standard two-fluid momentum exchange term that depends on $\mathbf{v}_{pg}$.

The purpose of the drag law is to close C_D, which depends on Re_p and other dimensionless parameters such as $\mathcal{M}_p$ and α_p. While drag laws accounting for Re_p are well-known due to extensive experimental and numerical data on an isolated particle [23], the extension to clustering effects (α_p) and compressibility of the carrier phase ($\mathcal{M}_p$) are still ongoing research topics. The drag coefficient $C_D(Re_p)$ can be obtained from the standard Schiller–Naumann expression:

$$C_D(Re_p) = \begin{cases} \frac{24}{Re_p}\left(1 + 0.15 Re_p^{0.687}\right), & \text{if } Re_p < Re_\infty \\ 0.44, & \text{otherwise} \end{cases} \tag{35}$$

where the maximum Reynolds is often taken as $Re_\infty = 1000$. Clustering effects are often introduced by a correction factor, which depends on α_g in the fashion of the Richardson–Zaki empirical relation [29] in the form α_g^n. However, this correlation was initially developed for incompressible flows. On the other hand, recent works provide a review of experimental data sets to model compressibility effects on the drag coefficient [20, 34]. Unfortunately, the resulting drag models do not account for the particle concentration. It is only recently that a drag model has been proposed to simultaneously account for Re_p, Ma_p and α_p [24]. These correlations are obtained from DNS of a shock interacting with a random array of fixed spheres and other data sets from previous simulations.

Drag model 1: Schiller–Naumann with Richardson–Zaki correction. The first model considered for drag is taken from [12]:

$$C_D(Re_p, \alpha_p) = C_D(Re_p)\alpha_g^{-2.65}. \tag{36}$$

This model consists of the Schiller–Naumann model with the Richardson–Zaki correction to account for volume-fraction effects.

Drag model 2: correlation from DNS. The second model considered for drag is taken from [24] and accounts for the compressibility of the carrier flow:

$$C_D(Re_p, \alpha_p, \mathcal{M}_p) = C_D(Re_p, \mathcal{M}_p)\alpha_g^{-1} + \frac{24}{Re_p}\alpha_g\,(b_1 + b_2) + b_3 \tag{37}$$

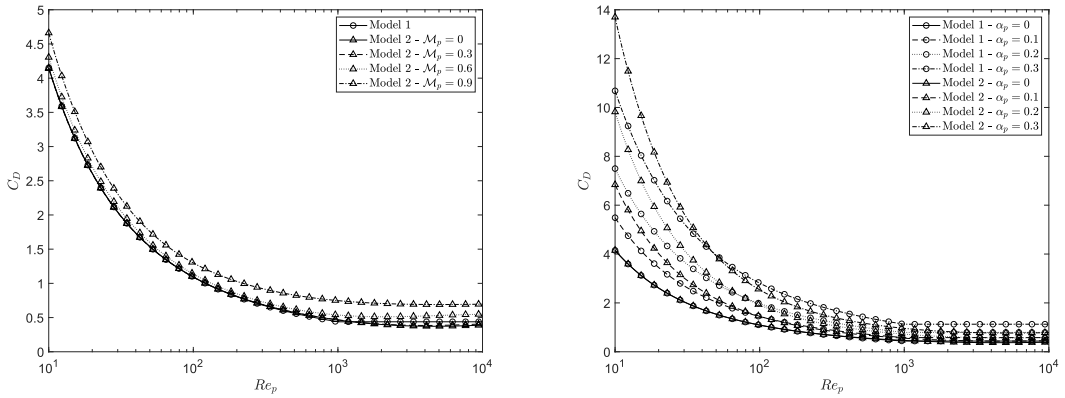

(a) Drag coefficient with $\alpha_p = 0$ and variable particle Mach number.

(b) Drag coefficient with $\mathcal{M}_p = 0$ and variable volume fraction.

Figure 1: Drag coefficient with respect to Re_p for different particle Mach numbers and volume fractions

with $C_D(Re_p, \mathcal{M}_p)$ a drag coefficient derived in [20] where different data sets have been compiled to provide a correlation for an isolated sphere experiencing flows in different regimes. This drag coefficient and the additional coefficients b_1, b_2 and b_3 are provided in Appendix A. The ranges of validity of this model are $Re_p \in [0.25, 300]$, $\alpha_p \in [0, 0.4]$, $\mathcal{M}_p \in [0, 1.2]$, which match with the configurations explored in this work.

The particle-Mach-number and particle-concentration dependencies are illustrated in figs. 1a and 1b, respectively. The particle Mach number tends to increase the drag coefficient with a simple shifting of the drag coefficient for the range met in this configurations (from 0 to 0.9). It is important to recall that the particle Mach number is based on the slip velocity, which is subsonic even with a high-speed gas because of the motion of the particles. Regarding the particle concentration, the two models scale differently with volume fraction and particle Reynolds number. While model 2 leads to a higher increase of the drag coefficient at low particle Reynolds number, the curves intersect with model 1 to provide a smaller drag coefficient for high particle Reynolds numbers.

3.2. Added-mass model

If we rewrite the added-mass volume fraction as $\alpha_a = c_m \alpha_g \alpha_p$ where $0 < c_m < 1$ is the added-mass coefficient with equilibrium value $c_m^\star$, then S_a can be modeled using

$$S_a = \frac{1}{\tau_a} \rho_g \alpha_g \alpha_p (c_m^\star - c_m). \tag{38}$$

The time scale for relaxation towards equilibrium τ_a is assumed to be proportional to the time scale for particle drag τ_p. It is then interesting to explore different possibilities for the definition of $c_m^\star$, which dictates the value that c_m needs to relax to at steady state. Added mass is an inviscid contribution and should not depend on the particle Reynolds number; however, it can depend on the particle Mach number because of its unsteady nature [17]. More specifically, it is expected to be predominant in the early times when the shock hits the curtain, the time scale for relaxation is then the acoustic time scale.

Added-mass model 1: Zuber. The first approach is taken from [41] where the value of $c_m^\star(\alpha_p)$ for a sphere in an incompressible inviscid flow is derived:

$$c_m^\star(\alpha_p) = 0.5 \min(1 + 2\alpha_p, 2). \tag{39}$$

Added-mass model 2: Parmar Mach correction. In [26], a numerical study is presented on the unsteady terms where the flow around a cylinder is compressible. In this case, the inviscid forces should tend to the same as for incompressible flows, but on a longer time scale. In the case of compressible flows, a correction is included to the model of Zuber

Table 3: Model constants used in the numerical study.

$$a_{min} = 0.5 \quad C_a = 1 \quad c_f = 0.01 \quad \alpha_{max} = 0.63 \quad \Delta_f = 0.01 \quad p_f = 533,333 \text{ kg/m/s}^2$$
$$\nu_g = 1.36 \times 10^{-5} \text{ m}^2/\text{s} \quad \gamma_g = 1.4 \quad \lambda_g = 0.0256 \text{ kg m/s}^3/\text{K} \quad C_{p,g} = 1300 \text{ m}^2/\text{s}^2/\text{K}$$

to account for the particle-Mach-number dependency:

$$c_m^\star(\alpha_p, \mathcal{M}_p) = 0.5 \min\Big((1 + 2\alpha_p)(1 + 1.8\mathcal{M}_p^2 + 7.6\mathcal{M}_p^4), 2\Big). \tag{40}$$

Note that this model is only valid for $\mathcal{M}_p < 0.6$, which is the case in the supersonic configurations considered in this paper. For hypersonic cases, the particle Mach number used to compute the above model is limited to 0.6.

3.3. Particle-fluid-particle pressure

A consequence of the kinetic theory model used in this work is the presence of an additional pressure tensor $\mathbf{P}_{pfp}$, which depends on the slip velocity. Usually, $tr(\mathbf{P}_{pfp})$ is very small compared to the gas pressure p_g, and therefore has essentially no effect on the fluid-phase speed of sound. Nonetheless, it is important for the particle phase, particularly for shock–particle-curtain interactions where the slip velocity is high. It is then expected that the coefficient C_{pfp} will have an impact on the curtain dynamics. In bubbly flows, $C_{pfp} = c_m^\star$ ensures hyperbolicity when $\rho_p \ll \rho_g$. However, it can take lower values in the case of gas–particle flows and three values of $C_{pfp} = 0, 0.2, 0.4$ are used in section 5 to showcase the effect of the pfp pressure on the curtain dynamics.

3.4. Summary of the model constants

Now that all the closures have been described, a complete summary is given in table 2. These models introduce a large number of physical constants needed for the simulations, some of which are provided in table 3. Note that the constants depending on the particle material (ρ_p, $C_{V,p}$, e_c and d_p) are provided later in the numerical setup as they vary with the configuration. However, because particle–particle collisions are relatively unimportant for thin particle curtains with $\alpha_p < 0.2$, the value of the restitution coefficient e_c plays no role in the curtain dynamics. This would not be the case for a thick curtain where compression leads to large regions with high α_p and strong collisions [3, 15].

4. Numerical setup

4.1. Solver description

The governing equations presented in section 2 are solved using a standard finite-volume method implemented in MATLAB. The solver was designed to accurately capture sharp particle fronts, preserve contact discontinuities, and ensure stability in all flow regimes. Following the pioneer work of [15], a combination of AUSM$^+$up scheme [19] for the particle phase, and HLLC scheme [36] for the fluid phase is employed to solve the hyperbolic part of the system. The source terms detailed in section 3 are treated analytically with operator splitting [3] to avoid stability issues due to temporal stiffness. The solver have been assessed on numerous verification test cases (see [3] for details).

4.2. Problem setup

The experimental setup of reference is the SNL multiphase shock tube, which has been used for a decade [37] to study shock–particle-curtain interactions in the dense regime. It has the advantage to provide the most recent measurements over a wide range of material density, high-speed flow regimes (from supersonic [6] to hypersonic [38]) and gas–solid regimes. In the experiment, the shock tube is filled with a high-pressure gas (driver gas) and a gas at ambient conditions (driven gas). The driver and driven sections are separated by a diaphragm, which is released to produce the shock. (See Appendix B for details.) An illustration of the experimental setup is provided in fig. 2a.

The shock Mach number $\mathcal{M}_s$, can be controlled by the pressure in the driver section p_4. The relation is given in eq. (B.1) where the subscript 1 corresponds to the driven state at ambient conditions and 4 the driver state at high

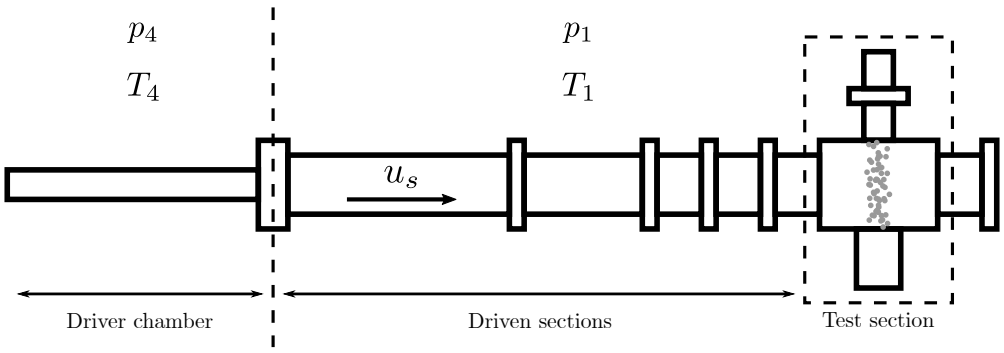

(a) Illustration of the experimental setup (not to scale).

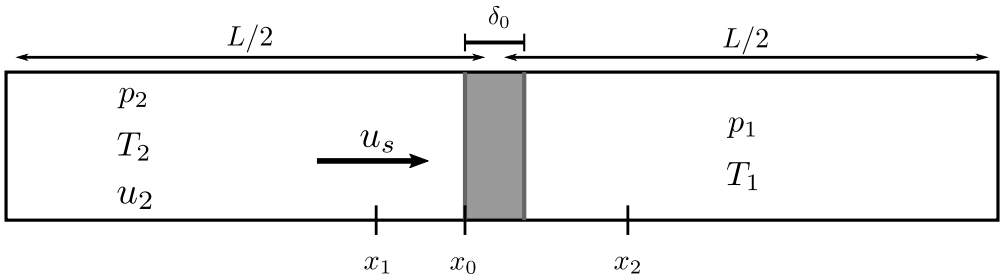

(b) 1-D numerical setup corresponding to the experiment.

Figure 2: Experimental (top) and numerical (bottom) setups corresponding to the SNL multiphase shock tube. x_0 is the location of the initial pressure discontinuity, while x_1 and x_2 correspond to the upstream and downstream pressure transducers used in the experiments. Finally, u_s corresponds to the shock speed and δ_0 is the initial curtain width (grey region).

Table 4: Summary of the physical and computational parameters used in the numerical setup.

p_1 (kPa)	T_1 (K)	p_2, T_2 and u_2	L	x_0 (mm)	x_1 (mm)	x_2 (mm)
84.1	297	eq. (B.2)	$100\delta_0$	$-\delta_0/2$	-31	31

pressure. Usually, hydrogen is used for the driver gas because it is easier to control its pressure, while ambient air is used in the driven section. To reproduce this experiment, the development of the shock is not of interest and requires a long upstream section to avoid the contact wave reaching the space and time frame of interest. This specific point is showcased in Appendix B where the contact wave produced by the pressure discontinuity interacts with the reflected shock wave and reaches the curtain before the end of the simulation. Instead, the zone upstream of the curtain is initialized with p_2, T_2 and u_2 corresponding to the post-shock quantities obtained by the exact shock relations of eq. (B.2) at a given $\mathcal{M}_s$. This results in starting the simulation at the very moment when the shock hits the curtain t_{shock}.

Note that this initialization methodology was also used in previous numerical studies [15, 18]. The driver gas is not expected to be relevant for the interaction with the curtain, both driver and driven gas are taken as air with $\gamma_1 = \gamma_2 = \gamma_4 = 1.4$. Then, the pre-shock quantities are taken as the ambient conditions $T_1 = 297$ K and $p_1 = 84.1$ kPa. This setup is quasi-1-D even if some 3-D effects due to the mechanical design limitations detailed in [37] are present. Hence, the computational domain is reduced to a 1-D shock tube. The shock tube is truncated to keep a minimal version where the driver and driven sections are reduced compared to the experiments. The length of the computational domain $L = 100\delta_0$ is taken such that the shock can develop without boundary effects. The number of cells in the curtain width N_c is prescribed, which imposes a minimum mesh size $\Delta x_{min} = \delta_0/N_c$ in the zone of interest. The curtain resolution $N_c = 40$ has been chosen such that the results are mesh independent after a mesh convergence study provided in Appendix C. The numerical setup is illustrated in fig. 2b with the parameters defined in table 4. The domain is defined as $[-L/2, L/2]$.

Table 5: Physical properties of the fluid and particle phases for shock–particle-curtain cases used in simulations.

Configuration	Material	ρ_p (kg/m^3)	$C_{V,p}$ (m^2/s^2/K)	e_c	d_p (μm)	δ_0 (mm)	α_p	$\mathcal{M}_s$
1	316 stainless steel	8170	500	0.75	115	1.7	0.17	1.4
2	316 stainless steel	8170	500	0.75	115	1.7	0.17	1.55
3	316 stainless steel	8170	500	0.75	115	1.7	0.17	1.7
4	Tungsten	17070	134	0.37	115	2.3	0.18	1.4
5	Tungsten	17070	134	0.37	115	2.3	0.18	1.55
6	Tungsten	17070	134	0.37	115	2.3	0.18	1.7
7	Cast stainless steel	7390	500	0.75	328	4.0	0.09	1.4
8	Cast stainless steel	7390	500	0.75	328	4.0	0.09	1.55
9	Cast stainless steel	7390	500	0.75	328	4.0	0.09	1.7
10	Soda lime glass	2520	840	0.97	115	1.6	0.19	1.4
11	Soda lime glass	2420	840	0.97	115	2.0	0.19	2.97
12	Soda lime glass	2420	840	0.97	115	2.0	0.19	4.24

Algorithm 1 Search of curtain edges from the α_p field.

$\mathcal{U} \leftarrow false$ ▷ Upstream edge is undetermined
$\mathcal{D} \leftarrow false$ ▷ Downstream edge is undetermined
for i in 1 to N_p **do** ▷ Loop over computational cells
  if $\alpha_{p,i} \geq 0.95\alpha_p^M$ and $\mathcal{U} = false$ **then**
    $\mathcal{U} \leftarrow true$ ▷ Upstream edge has been found
    $x_{ups} \leftarrow x_i$
  end if
  if $\alpha_{p,i} \leq 0.95\alpha_p^M$ and $\mathcal{U} = true$ and $\mathcal{D} = false$ **then**
    $x_{dws} \leftarrow x_i$
    break ▷ Downstream edge has been found. Exit loop
  end if
end for

The data used in this work [6, 38] have the advantage of compiling a wide range of material densities, curtain widths, particle concentrations and gas-flow regimes. Indeed, the most recent configurations have supersonic shocks, which have not yet been studied extensively. The configuration list is given in table 5 where the particle diameters d_p are taken as the mean between the minimum and maximum diameter provided in the experiment. In Appendix D, a study is provided to test the sensitivity of the results to this parameter. Usually, it is admitted that the relevant length scale should be δ_0 instead of d_p for this particular application [4].

4.3. Post-processing

The determination of curtain edges can be ambiguous because it depends on some ad-hoc considerations. This has already been discussed in [15] where several α_p isocontours are displayed, which correspond to very different curtain-edge evolution with time. In the two references used here [6, 38], the curtain edges were taken as 95% of the maximum pixel intensity. Here, the same metric is used where the pixel intensity corresponds to the maximum volume fraction in the domain at a given time. In practice, the curtain edges, i.e., the upstream edge x_{ups} and the downstream edge x_{dws} are determined for an instantaneous α_p field by following the steps of algorithm 1. Then, the curtain width is simply computed as $\delta = x_{dws} - x_{ups}$. Apart from that, the gas pressures at x_1 and x_2 are also saved in time to compare with the pressure measurements obtained in the experiments.

4.4. Reduction of computational time

The numerical setup needs to allow for a large number of simulations in a reasonable computational time. In order to optimize the numerical setup, several adjustments were made on the domain size, the mesh refinement and the

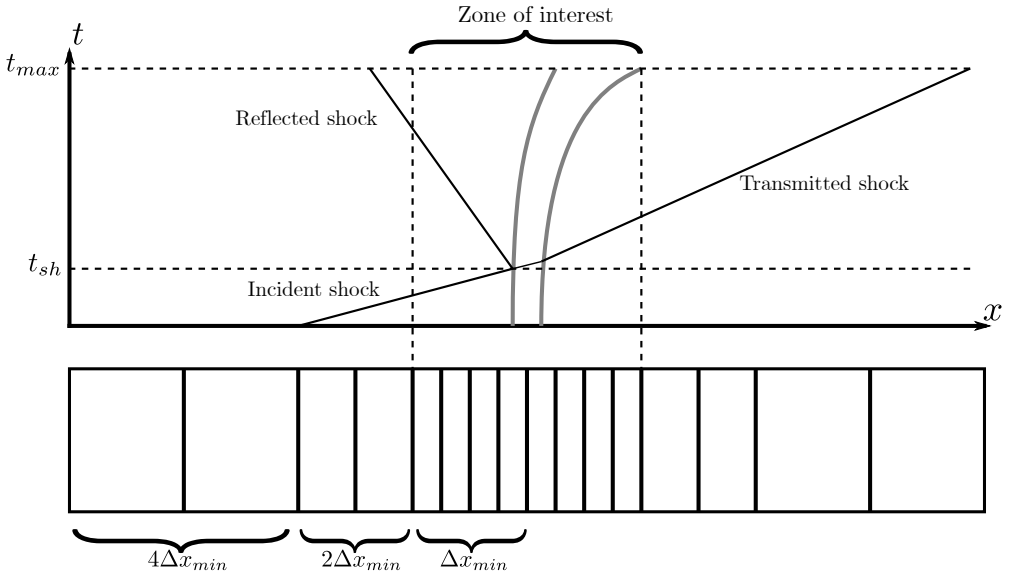

Figure 3: Schematic x–t diagram of the shock interacting with the curtain. When the diaphragm is released, an incident shock and a contact surface propagate towards the curtain. A part of the incident shock is reflected by the curtain and the remaining part is transmitted across the curtain. The mesh is also represented to illustrate the refinement strategy in the zone of interest.

numerical method. Even with the optimal domain size, the zone of interest is restrained to a small part of the shock tube where the curtain is moving during the measurement time frame. The choice here is to use a tree-based mesh coarsening outside of the curtain zone as depicted in fig. 3.

In an intermediate zone where the incident shock develops, the mesh size is $2\Delta x_{min}$. Finally, the coarsening is even more important in the zone before x_0 with a mesh size of $4\Delta x_{min}$. This treatment leads to a significant speedup of simulations without loss of accuracy. Finally, the high-order scheme used in the original version of the code [3] is replaced by a simple first-order scheme in space and time to decrease computational time without significant loss of accuracy.

5. Results

This section provides more details on the effect of modeling choices for the inter-phase exchange terms. While in [18], the parametric study was focused on the physical parameters such as shock Mach number, particle diameter and curtain thickness, the studies in this work explore the sensitivity of the results regarding the models for drag, added mass and pfp pressure. For convenience, the results are made dimensionless, using the characteristic length of the problem δ_0 and a scaling time t^*, which was proposed in [18]:

$$t^* = \alpha_p^{-0.25} \frac{\delta_0}{u_2} \sqrt{\frac{\rho_2}{\rho_p}} \tag{41}$$

with ρ_2 and u_2 the density and velocity in the post-shock region obtained from the relations in eq. (B.2).

5.1. Physical description

This first study aims to provide a detailed description of the physics of shock–particle-curtain interactions by focusing on configuration 1 of table 5. This case is also detailed in the results section of [6] where a temporal pressure evolution is given at the two locations x_1 and x_2 represented in fig. 2b. The x–t diagram of density is given in fig. 4a, which shows the expected behavior illustrated in fig. 3. Indeed, a part of the incident shock is reflected and the transmitted shock is weakened. This behavior can also been described by the two pressure probes located at x_1 and

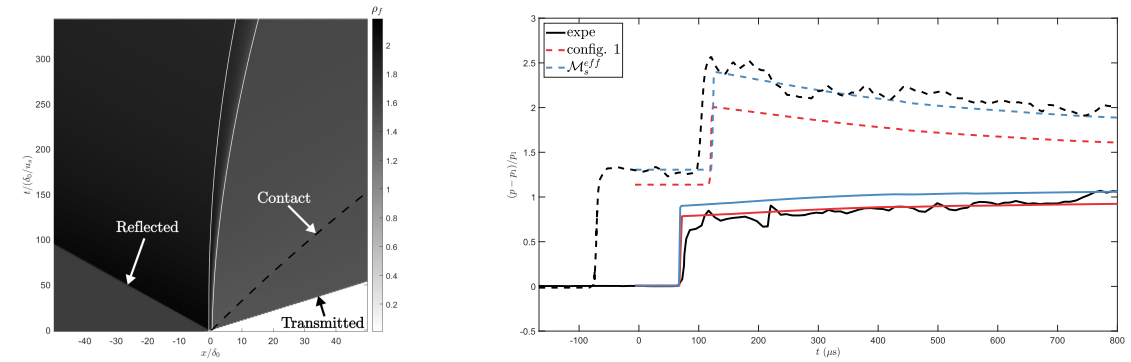

(a) x–t diagram of density for configuration 1.

(b) Temporal evolution of pressure for configuration 1.

Figure 4: In (a), the x–t diagram of density is represented with the isocontour of α_p taken as 5% of the maximum α_p value. In (b), the two curves correspond to the locations of the two pressure probes.

x_2, which measure the intensity of the shock upstream and downstream of the curtain, respectively. Also, a contact discontinuity is transmitted across the curtain, which was also observed in the literature [18].

In fig. 4b, it can be seen that the post-shock pressure captured by the sensor of the experiment does not equal the exact pressure p_2 corresponding to $\mathcal{M}_s = 1.4$. This could be explained by 3-D effects or experimental inaccuracy in the definition of the shock Mach number $\mathcal{M}_s$. In [6], a scaling law was proposed based on the measured pressures at x_1 and x_2, instead of the post-shock velocity u_2. This scaling law was able to better collapse the different curves, especially for configurations with relatively low $\mathcal{M}_s$. This concurs with the idea that the $\mathcal{M}_s$ provided in the experimental setup might be underestimated or that 3-D geometry effects might produce a faster effective shock in the shock tube. By computing an effective Mach number $\mathcal{M}_s^{eff} \simeq 1.45$ based on the post-shock pressure experimentally measured at x_1, the same case has been simulated and corresponds to the curve $\mathcal{M}_s^{eff}$ in fig. 4b. The correct pressure at x_1 is then retrieved, even if the reflected shock speed seems to be slower than what was measured in the experiments.

Now that the first configuration has been presented, several modeling choices are explored for the full parameter space and the curtain spreading rate is compared to the experimental data. Note that in the following study, some results differ from the experimental data for the reasons explained above and due to the particle size distribution discussed in Appendix D. However, this does not prevent us from studying the effect of modeling choices on the curtain dynamics. In the following, we use the value of $\mathcal{M}_s$ reported in the experiments instead of $\mathcal{M}_s^{eff}$, although the latter would better match the experimental results for the spreading rate.

5.2. Drag-model study

As detailed in section 3.1, drag models can have different levels of complexity to account for particle clustering and high-speed effects. Nonetheless, for shock–particle interactions the drag model represents the principal force accelerating the particles. Hence, our first study focuses on the drag models for high-speed flows and dense granular phases. In this study, the entire batch of configurations given in table 5 are simulated to analyze the impact of the drag model over a wide parameter space. We should note that the particle Mach number $\mathcal{M}_p$, which depends on the slip velocity, will be smaller than the shock Mach number $\mathcal{M}_s$. Thus, for example, $\mathcal{M}_s$ must be sufficiently large before $\mathcal{M}_p$ has a significant effect on the drag coefficient.

For the four materials in figs. 5 to 8, we observe that the temporal evolution of the curtain width is fairly well reproduced regarding the observations of section 5.1 and Appendix D. The difference between the drag model with and without $\mathcal{M}_p$ dependency is most visible for high-speed flows, high concentration and small material density. Indeed, in fig. 6, the drag model has only minor impact on the curtain spreading rate, while in fig. 7 drag model 2 allows to approach better the experimental data. Also, it is interesting to observe that drag model 1 predicts higher spreading rates for low-speed flows, while the opposite happens for larger Mach numbers in figs. 5, 6 and 8. This observation shows the complexity of compressibility effects on the drag experienced by particles. Overall, the use of a DNS-based model accounting for the $\mathcal{M}_p$ dependency allows to better predict the physical behavior.

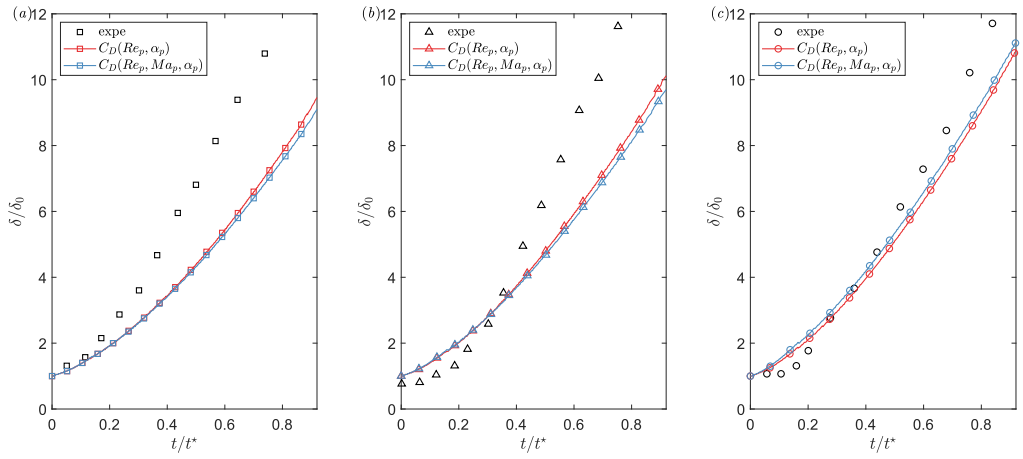

Figure 5: Effect of drag model on width evolution in time of a curtain composed of 316 stainless steel particles for $\mathcal{M}_s = 1.4$ (a), $\mathcal{M}_s = 1.55$ (b) and $\mathcal{M}_s = 1.7$ (c). δ_0 is the initial curtain width and t^* is the characteristic time given by eq. (41).

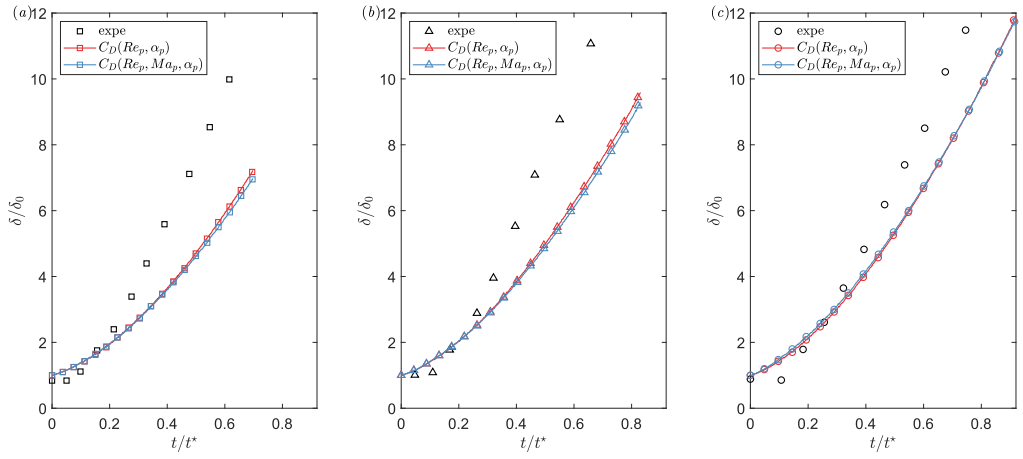

Figure 6: Effect of drag model on width evolution in time of a curtain composed of tungsten particles for $\mathcal{M}_s = 1.4$ (a), $\mathcal{M}_s = 1.55$ (b) and $\mathcal{M}_s = 1.7$ (c). δ_0 is the initial curtain width and t^* is the characteristic time given by eq. (41).

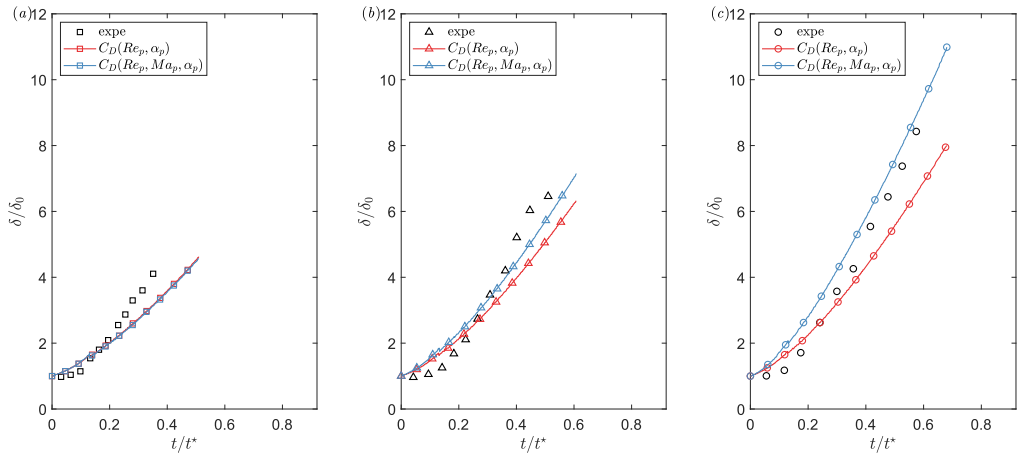

Figure 7: Effect of drag model on width evolution in time of a curtain composed of cast stainless steel particles for $\mathcal{M}_s = 1.4$ (a), $\mathcal{M}_s = 1.55$ (b) and $\mathcal{M}_s = 1.7$ (c). δ_0 is the initial curtain width and t^* is the characteristic time given by eq. (41).

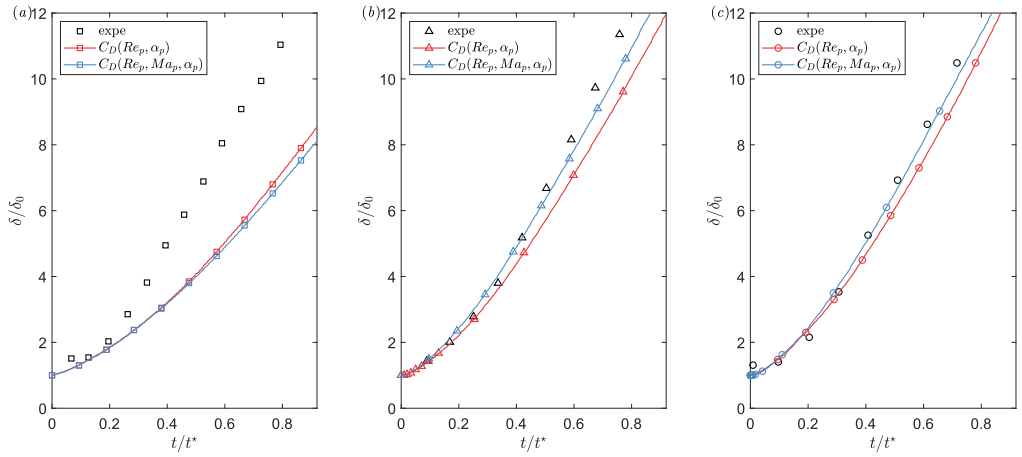

Figure 8: Effect of drag model on width evolution in time of a curtain composed of soda lime glass particles for $\mathcal{M}_s = 1.4$ (a), $\mathcal{M}_s = 2.97$ (b) and $\mathcal{M}_s = 4.24$ (c). δ_0 is the initial curtain width and t^* is the characteristic time given by eq. (41).

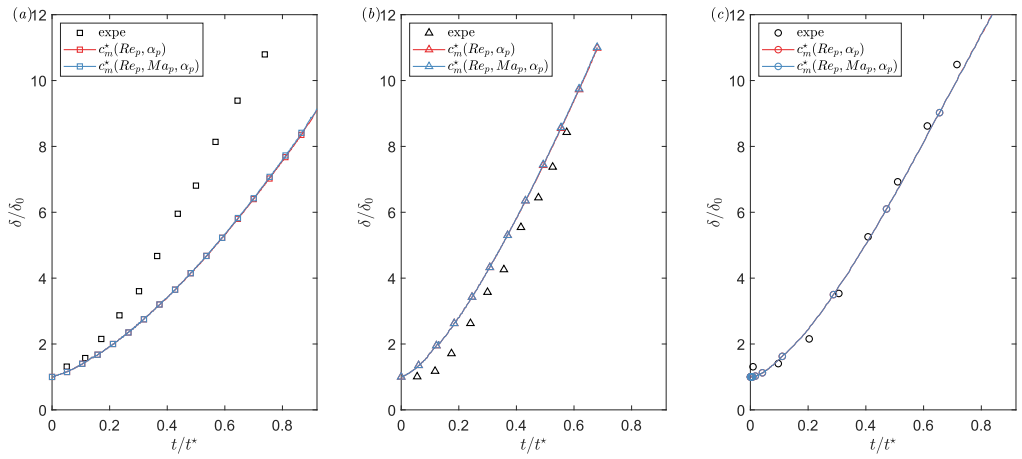

Figure 9: Effect of added-mass model on width evolution in time for configurations 1, 9 and 12. δ_0 is the initial curtain width and t^* is the characteristic time given by eq. (41).

5.3. Added-mass-model study

The effect of the added-mass model has been explored in the context of Lagrangian particles in [18], and is studied here where the inclusion of the added mass in the two-fluid model is novel. The two models presented in section 3.2 are then compared on three configurations in fig. 9. As it can be observed, the added-mass model does not impact the curtain dynamics even at early stages. The same conclusion can be drawn for the other configurations not displayed here. This result can be explained by the large density ratio between the particles and the gas. Indeed, the unsteady-force effects on the particle velocity (curtain spreading rate) have been demonstrated to be inversely proportional to the particle-to-fluid density ratio in [17]. The modeling of this term is more crucial for sedimentation problems or bubbly flows where this density ratio is much lower [3].

5.4. pfp-pressure-model study

While P_{pfp} has an important role in the hyperbolicity of the two-fluid model, it can also impact the particle dynamics in the presence of important volume fraction gradients or high slip velocity. When the shock hits the curtain, the upstream edge experiences a huge rise in slip velocity in a zone of rapid variation of volume fraction. It is then expected that the modeling of C_{pfp} modifies the evolution in time of the upstream curtain edge specifically. After the shock has passed through the particle curtain, the slip velocity can still be quite large, causing the particles to be pushed apart due to the pfp pressure. In this study, the trajectories of the edges are plotted in figs. 10 to 13 instead of the curtain width to better showcase the separate evolution of the upstream and downstream curtain positions.

As expected, the pfp pressure has the effect of spreading the curtain in all the configurations. When the magnitude of C_{pfp} is increased, the spreading rate is even more important. It is also interesting to notice that the upstream edge is more affected than the downstream edge. More specifically, the curtain goes backward in the intermediate stages of the motion when $C_{pfp} = 0.4$. This effect is more visible for the stainless steel particles in fig. 12, which can be explained by the larger particle size leading to a larger slip velocity.

6. Conclusions

This work has been dedicated to the modeling of high-speed flow interacting with thin particle curtains. The EE two-fluid model includes four-way coupling (Archimedes' forces, collisions and friction), added mass, inter-phase heat exchange and pseudo-turbulence of the fluid induced by the particle motion. The well-established experimental setup for shock–particle interactions developed at SNL is used as a reference to explore the modeling of drag, added mass and pfp pressure. A cross-sample of two experimental campaigns from [6] and [38] is used to explore a large range of shock Mach numbers, particle concentrations and material densities.

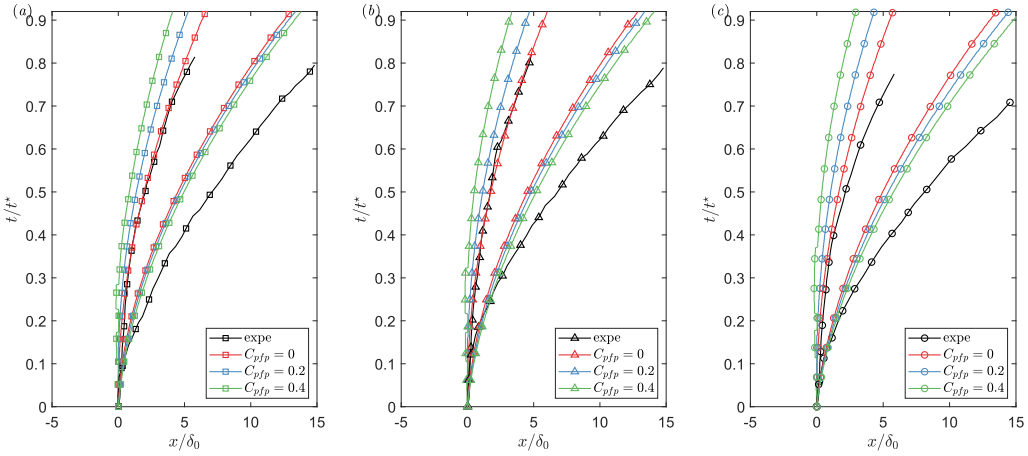

Figure 10: Effect of pfp pressure on trajectories of upstream and downstream edges of a curtain composed of 316 stainless steel particles for $\mathcal{M}_s = 1.4$ (a), $\mathcal{M}_s = 1.55$ (b) and $\mathcal{M}_s = 1.7$ (c). δ_0 is the initial curtain width and t^* is the characteristic time given by eq. (41)).

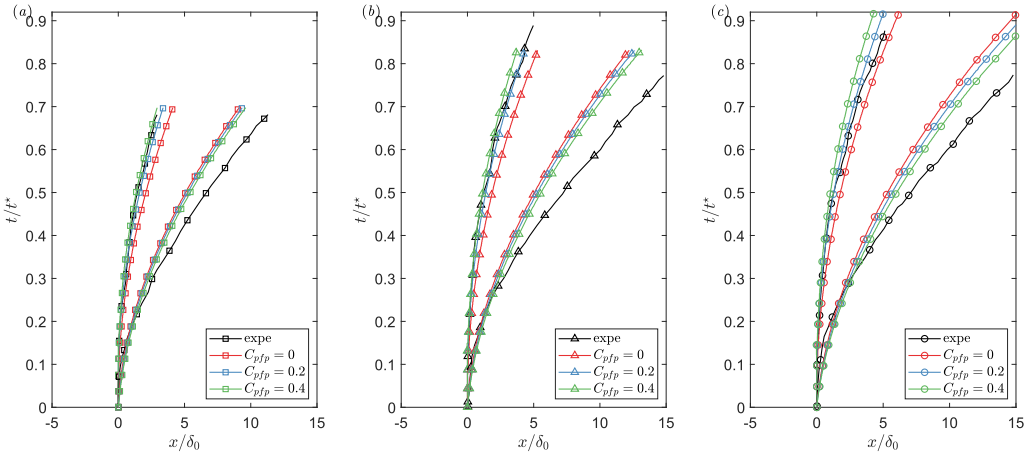

Figure 11: Effect of pfp pressure on trajectories of upstream and downstream edges of a curtain composed of tungsten particles for $\mathcal{M}_s = 1.4$ (a), $\mathcal{M}_s = 1.55$ (b) and $\mathcal{M}_s = 1.7$ (c). δ_0 is the initial curtain width and t^* is the characteristic time given by eq. (41). Each colored curve represent a drag model.

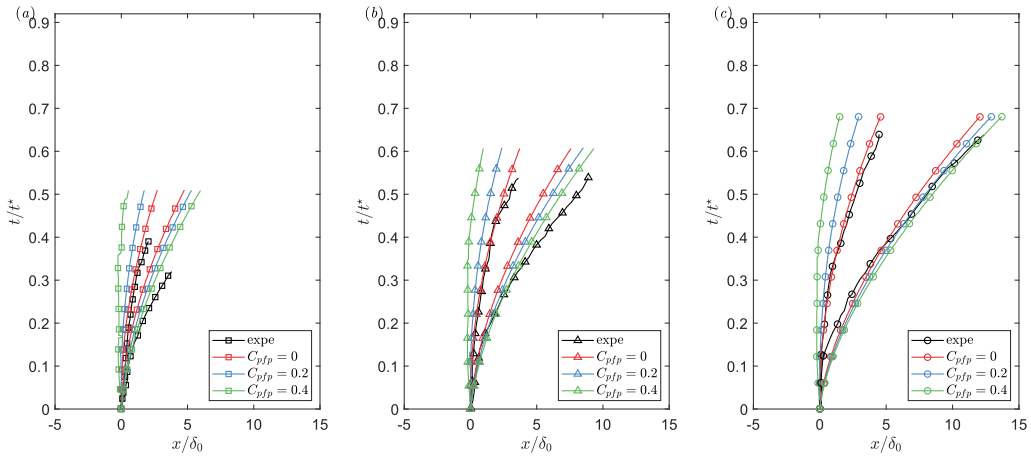

Figure 12: Effect of pfp pressure on trajectories of upstream and downstream edges of a curtain composed of cast stainless steel particles for $\mathcal{M}_s = 1.4$ (a), $\mathcal{M}_s = 1.55$ (b) and $\mathcal{M}_s = 1.7$ (c). δ_0 is the initial curtain width and t^* is the characteristic time given by eq. (41).

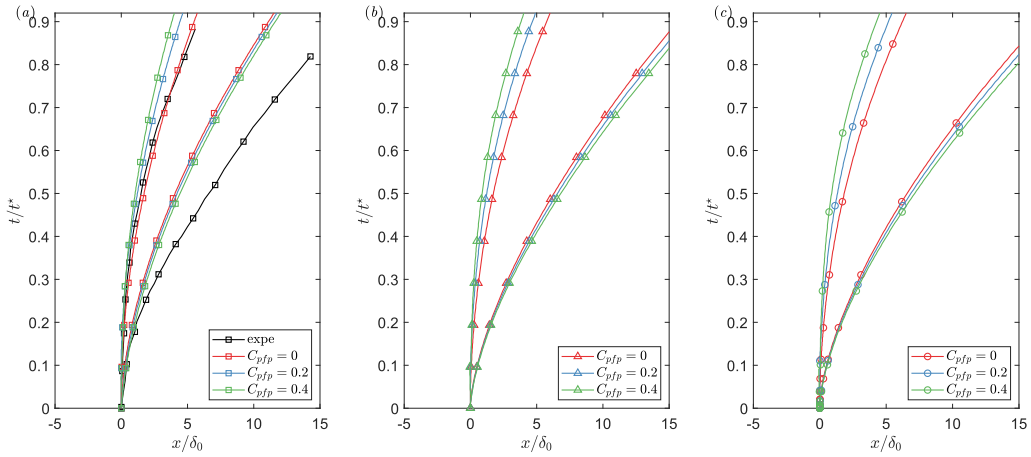

Figure 13: Effect of pfp pressure on trajectories of upstream and downstream edges of a curtain composed of soda lime glass particles for $\mathcal{M}_s = 1.4$ (a), $\mathcal{M}_s = 2.97$ (b) and $\mathcal{M}_s = 4.24$ (c). δ_0 is the initial curtain width and t^* is the characteristic time given by eq. (41).

Overall, the curtain spreading rate is reproduced with reasonable accuracy by the two-fluid model. Some discrepancies are found for the configurations with the smallest Mach numbers, even if these differences could be due to 3-D effects or the particle size distribution. Indeed, it has been shown from the most detailed case that the gas pressure was over-estimated at the upstream probe (or the shock Mach number was under-estimated). This finding does not invalidate the subsequent study about the models for inter-phase exchanges. The impact of several modeling parameters such as the drag coefficient, the added-mass coefficient, and the magnitude of the pfp pressure is also investigated.

For thin particle curtains, it was found that the complete drag model accounting for Re_p, $\mathcal{M}_p$ and α_p is more accurate compared to previous drag models depending on Re_p and α_p only. While the complete drag model leads to an increased spreading rate for most of the configurations, this is not the case for the low-speed configurations. Overall, the difference between the drag models is more predominant for high-speed flows, high particle concentrations and small material density. On the other hand, the added-mass model has no impact on the results. This is in agreement with the analysis in [17] stating that this force is inversely proportional to the particle-to-fluid density ratio. In the case of gas–particle systems, this ratio is usually very large and added mass is not expected to greatly affect the particle acceleration.

In contrast, the magnitude of the pfp pressure has a real impact on the spreading rate of the curtain. Indeed, for moderately dense curtains with large slip velocity, the pfp pressure can be much larger than the collisional pressure, especially for $e_c \ll 1$. In any case, all contributions to the particle pressure lead to increased spreading as they work to push particles towards regions of lower particle-phase pressure. This shows an interesting feature of the two-fluid model: the pfp pressure from kinetic theory not only cures the historical issue of hyperbolicity, but also captures a physical effect with visible impact on the dynamics of the granular phase in high-speed flows.

The two-fluid model used in this work is able to reproduce the curtain dynamics fairly accurately in a small amount of computational time (about one hour of CPU time for each 1-D configuration). It is thus a useful tool to expend the parametric space to higher-speed flows and denser curtains, which are more difficult to capture experimentally. Future works could focus on exploring configurations that have not yet been measured experimentally and on improving the scaling models. Also, 3-D simulations could be envisioned to account for hidden contributions, which could explain the discrepancies between the 1-D simulations and the experiments. The particle size distribution in the experiments is not completely monodisperse and it would be interesting to employ the kinetic-based framework to develop a polydisperse model to include such size-dependent physics. Finally, the two-fluid model could be applied to other dispersed two-phase systems where buoyancy terms and added mass are expected to be predominant such as sedimentation or bubbly flows [3, 11].

Acknowledgments

When preparing this work, ROF was supported by the Fulbright–Tocqueville Distinguished Chair Award and the Jean D'Alembert Senior Professor Chair at the Université de Paris-Saclay. The Government of the United States or any agency representing it has not endorsed the conclusions or approved the contents of this publication.

References

[1] M. R. Baer and J. W. Nunziato. A two-phase mixture theory for the deflagration-to-detonation transition (DDT) in reactive granular materials. International Journal of Multiphase Flow, 12(6):861–889, 1986.

[2] P. L. Bhatnagar, E. P. Gross, and M. Krook. A model for collision processes in gases. I. Small amplitude processes in charged and neutral one-component systems. Physical Review, 94(3):511, 1954.

[3] V. Boniou, R. O. Fox, and F. Laurent. A kinetic-based model for high-speed, monodisperse, fluid–particle flows. HAL preprint https://hal.science/hal-04037062, 2023.

[4] J. Capecelatro and J. L. Wagner. Gas-particle dynamics in high-speed flows. arXiv preprint arXiv:2303.00825, 2023.

[5] T. L. Cook and F. H. Harlow. Virtual mass in multiphase flow. International Journal of Multiphase Flow, 10(6):691–699, 1984.

[6] K. A. Daniel and J. L. Wagner. The shock-induced dispersal of particle curtains with varying material density. International Journal of Multiphase Flow, 152:104082, 2022.

[7] E. P. DeMauro, J. L. Wagner, L. J. DeChant, S. J. Beresh, and A. M. Turpin. Improved scaling laws for the shock-induced dispersal of a dense particle curtain. Journal of Fluid Mechanics, 876:881–895, 2019.

[8] L. J. Forney, D. B. Van Dyke, and W. K. McGregor. Dynamics of particle-shock interactions. Part I: similitude. Aerosol Science and Technology, 6(2):129–141, 1987.

[9] L. J. Forney, A. E. Walker, and W. K. McGregor. Dynamics of particle-shock interactions. Part II: effect of the Basset term. Aerosol Science and Technology, 6(2):143–152, 1987.

[10] R. O. Fox. A kinetic-based hyperbolic two-fluid model for binary hard-sphere collisions. Journal of Fluid Mechanics, 877:282–329, 2019.
[11] R. O. Fox, F. Laurent, and A. Vié. A hyperbolic two-fluid model for compressible flows with arbitrary material-density ratios. Journal of Fluid Mechanics, 903:A5, 2020.
[12] D. Gidaspow. Multiphase Flow and Fluidization: Continuum and Kinetic Theory Descriptions. Academic Press, New York, USA, 1994.
[13] D. J. Gunn. Transfer of heat or mass to particles in fixed and fluidized beds. International Journal of Heat and Mass Transfer, 21:467–476, 1978.
[14] Z. Hosseinzadeh-Nik, S. Subramaniam, and J. D. Regele. Investigation and quantification of flow unsteadiness in shock-particle cloud interaction. International Journal of Multiphase Flow, 101:186–201, 2018.
[15] R. W. Houim and E. S. Oran. A multiphase model for compressible granular–gaseous flows: Formulation and initial tests. Journal of Fluid Mechanics, 789:166–220, 2016.
[16] D. Lhuillier, C.-H. Chang, and T. G. Theofanous. On the quest for a hyperbolic effective-field model of disperse flows. Journal of Fluid Mechanics, 731:184–194, 2013.
[17] Y. Ling, A. Haselbacher, and S. Balachandar. Importance of unsteady contributions to force and heating for particles in compressible flows. Part 1: Modeling and analysis for shock–particle interaction. International Journal of Multiphase Flow, 37(9):1026–1044, 2011.
[18] Y. Ling, J. L. Wagner, S. J. Beresh, S. P. Kearney, and S. Balachandar. Interaction of a planar shock wave with a dense particle curtain: Modeling and experiments. Physics of Fluids, 24(11):113301, 2012.
[19] M.-S. Liou. A sequel to AUSM, Part II: AUSM$^+$-up for all speeds. Journal of Computational Physics, 214(1):137–170, 2006.
[20] E. Loth, J. T. Daspit, M. Jeong, T. Nagata, and T. Nonomura. Supersonic and hypersonic drag coefficients for a sphere. AIAA Journal, 59(8):3261–3274, 2021.
[21] M. Mehrabadi, S. Tenneti, R. Garg, and S. Subramaniam. Pseudo-turbulent gas-phase velocity fluctuations in homogeneous gas-solid flow: fixed particle assemblies and freely evolving suspensions. Journal of Fluid Mechanics, 770:210–246, 2015.
[22] Y. Mehta, T. L. Jackson, and S. Balachandar. Pseudo-turbulence in inviscid simulations of shock interacting with a bed of randomly distributed particles. Shock Waves, 30:49–62, 2020.
[23] Z. Naumann and L. Schiller. A drag coefficient correlation. Zeitschrift des Vereins Deutscher Ingenieure, 77(318):e323, 1935.
[24] A. N. Osnes, M. Vartdal, M. Khalloufi, J. Capecelatro, and S. Balachandar. Comprehensive quasi-steady force correlations for compressible flow through random particle suspensions. International Journal of Multiphase Flow, page 104485, 2023.
[25] A. N. Osnes, M. Vartdal, M. G. Omang, and B. A. P. Reif. Computational analysis of shock-induced flow through stationary particle clouds. International Journal of Multiphase Flow, 114:268–286, 2019.
[26] M. Parmar, A. Haselbacher, and S. Balachandar. On the unsteady inviscid force on cylinders and spheres in subcritical compressible flow. Philosophical Transactions of the Royal Society A: Mathematical, Physical and Engineering Sciences, 366(1873):2161–2175, 2008.
[27] A. Passalacqua, J. E. Galvin, P. Vedula, C. M. Hrenya, and R. O. Fox. A quadrature-based kinetic model for dilute non-isothermal granular flows. Communications in Computational Physics, 10(01):216–252, 2011.
[28] Y. E. Poroshyna and P. S. Utkin. Numerical simulation of a normally incident shock wave–dense particles layer interaction using the Godunov solver for the Baer–Nunziato equations. International Journal of Multiphase Flow, 142:103718, 2021.
[29] J. F. Richardson and W. N. Zaki. Sedimentation and fluidisation: Part I. Chemical Engineering Research and Design, 75:S82–S100, 1997.
[30] X. Rogue, G. Rodriguez, J. F. Haas, and R. Saurel. Experimental and numerical investigation of the shock-induced fluidization of a particles bed. Shock Waves, 8(1):29–45, 1998.
[31] R. Saurel and R. Abgrall. A multiphase Godunov method for compressible multifluid and multiphase flows. Journal of Computational Physics, 150(2):425–467, 1999.
[32] R. Saurel, A. Chinnayya, and Q. Carmouze. Modelling compressible dense and dilute two-phase flows. Physics of Fluids, 29(6):063301, 2017.
[33] G. S. Shallcross, R. O. Fox, and J. Capecelatro. A volume-filtered description of compressible particle-laden flows. International Journal of Multiphase Flow, 122:103138, 2020.
[34] N. Singh, M. Kroells, C. Li, E. Ching, M. Ihme, C. J. Hogan, and T. E. Schwartzentruber. General drag coefficient for flow over spherical particles. AIAA Journal, 60(2):587–597, 2022.
[35] T. G. Theofanous, V. Mitkin, and C.-H. Chang. The dynamics of dense particle clouds subjected to shock waves. Part 1. Experiments and scaling laws. Journal of Fluid Mechanics, 792:658–681, 2016.
[36] E. F. Toro, M. Spruce, and W. Speares. Restoration of the contact surface in the HLL-Riemann solver. Shock Waves, 4(1):25–34, 1994.
[37] J. L. Wagner, S. J. Beresh, S. P. Kearney, W. M. Trott, J. N. Castanada, B. O. Pruett, and M. R. Baer. A multiphase shock tube for shock wave interactions with dense particle fields. Experiments in Fluids, 52:1507–1517, 2012.
[38] J. L. Wagner, K. Daniel, C. Downing, T. W. Grasser, and K. P. Lynch. Shock–particle-curtain interactions at high Mach number. In AIAA SCITECH 2023 Forum, page 2303, 2023.
[39] M. Wang, Y. Yang, D. Z. Zhang, and S. Balachandar. Numerical calculation of the particle–fluid–particle stress in random arrays of fixed particles. Physical Review Fluids, 6:104306, 2021.
[40] P. K Zhang, H. W. Zhang, Y. F. Zhang, S. P. Li, and Q. Y. Meng. Modeling particle collisions in moderately dense curtain impacted by an incident shock wave. Physics of Fluids, 35(2):023327, 2023.
[41] N. Zuber. On the dispersed two-phase flow in the laminar flow regime. Chemical Engineering Science, 19(11):897–917, 1964.

Appendix A. Coefficients for drag models

In eq. (37), several coefficients are used to compute the drag models. In [20], the drag coefficient for an isolated sphere is given by

$$C_D(Re_p, \alpha_p, \mathcal{M}_p) = C_D(Re_p) l_1 + \frac{0.42 l_2}{1 + 42,500 Re_p^{-1.16 l_2} + l_3 Re_p^{-0.5}} \tag{A.1}$$

with

$$\begin{aligned}
l_1 &= \begin{cases} 0.0239\mathcal{M}_p^3 + 0.212\mathcal{M}_p^2 - 0.074\mathcal{M}_p^1, & \text{if } \mathcal{M}_p < 1 \\ 0.93 + \frac{1}{3.5 + \mathcal{M}_p^5}, & \text{otherwise} \end{cases} \\
l_2 &= \begin{cases} 1.65 + 0.65\tanh(4\mathcal{M}_p - 3.4), & \text{if } \mathcal{M}_p < 1.5 \\ 2.18 - 0.13\tanh(0.9\mathcal{M}_p - 2.7), & \text{otherwise} \end{cases} \\
l_3 &= \begin{cases} 1.66\mathcal{M}_p^3 + 3.29\mathcal{M}_p^2 - 10.9\mathcal{M}_p + 20, & \text{if } \mathcal{M}_p < 0.8 \\ 5 + 40\mathcal{M}_p^{-3}, & \text{otherwise} \end{cases}
\end{aligned} \tag{A.2}$$

The coefficients defined in [24] are

$$\begin{aligned}
b_1 &= 5.81\alpha_p\alpha_g^{-2} + 0.48\alpha_p^{1/3}\alpha_g^{-3} \\
b_2 &= \alpha_g^2\alpha_p^3 Re_p \left(0.95 + 0.61\alpha_g^{-2}\alpha_p^3\right) \\
b_3 &= \min\left(\sqrt{20\mathcal{M}_p}, 1\right)\left(5.65\alpha_p - 22\alpha_p^2 + 23.4\alpha_p^3\right)\left[1 + \tanh\left(\frac{\mathcal{M}_p - (0.65 - 0.24\alpha_p)}{0.35\alpha_p}\right)\right]
\end{aligned} \tag{A.3}$$

Appendix B. Shock relations and impact of initialization

This appendix aims to showcase the impact of initialization on the shock–curtain interaction. The first approach is to start the simulation with the pressure discontinuity of the experiment and let the shock develop until it reaches the curtain. Then, the pressure p_4 is obtained with the relation:

$$\frac{p_4}{p_1} = \frac{1 + \frac{2\gamma_1}{\gamma_1+1}(\mathcal{M}_s^2 - 1)}{\left(1 - \frac{\gamma_4-1}{\gamma_1+1}\frac{c_1}{c_4}\frac{\mathcal{M}_s^2-1}{\mathcal{M}_s}\right)^{\frac{2\gamma_4}{\gamma_4-1}}} \tag{B.1}$$

where c is the speed of sound while γ is the heat capacity ratio of the gas. Note that the relation considers different γ for the driver and driven gases because they are often different in experiments. In the simulation, both gases are taken as air with $\gamma_4 = \gamma_1 = 1.4$.

The other option is to directly initiate the simulation with the post-shock conditions. In this case, the shock does not need to develop and can be located just upstream of the curtain. The shock relations for a shock propagating in a quiescent gas are

$$\begin{aligned}
\frac{p_2}{p_1} &= \frac{2\gamma_1\mathcal{M}_s^2 - \gamma_1 + 1}{\gamma_1 + 1}, \\
\frac{T_2}{T_1} &= \frac{(2\gamma_1\mathcal{M}_s^2 - \gamma_1 + 1)(\mathcal{M}_s^2(\gamma_1 - 1) + 2)}{\mathcal{M}_s^2(\gamma_1 + 1)^2}, \\
\mathcal{M}_{2'}^2 &= \frac{2 + (\gamma_1 - 1)\mathcal{M}_s^2}{2\gamma_1\mathcal{M}_s^2 - \gamma_1 + 1}, \\
u_2 &= c_1\mathcal{M}_s - c_2\mathcal{M}_{2'}.
\end{aligned} \tag{B.2}$$

In this appendix, three ways of initializing the simulations are explored:

1. Use the pressure ratio given by eq. (B.1) with the discontinuity located at $x_0 = -3L/4$.

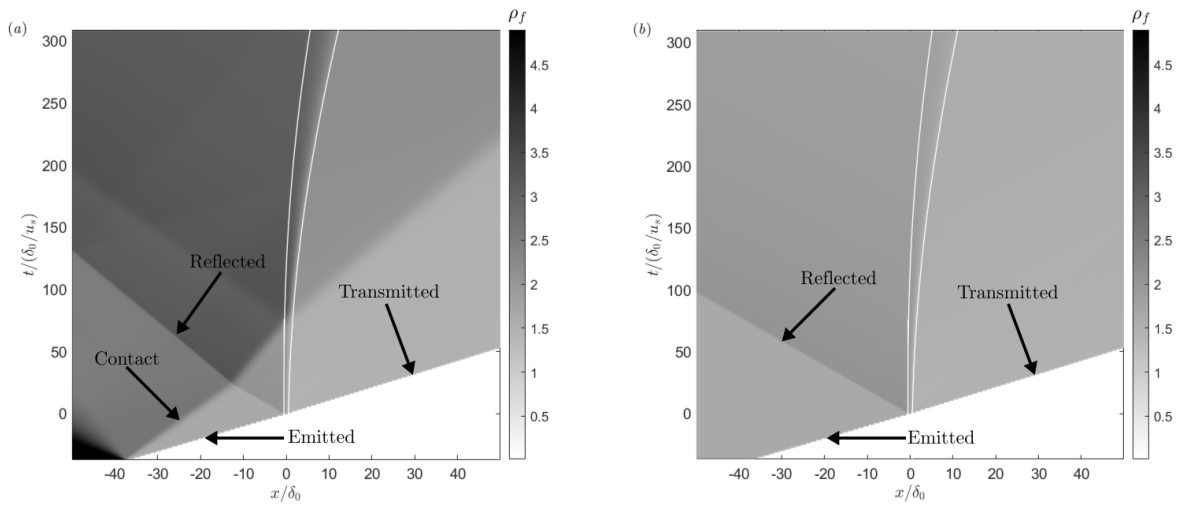

Figure B.14: Diagram x–t of density and volume fraction isocontour for shock-tube relations (a) and exact shock relations (b) used as initialization for configuration 1. A contact wave is produced for initialization 1 while this is not the case in initialization 2.

2. Use the exact shock relations from eq. (B.2) with the discontinuity located at $x_0 = -3L/4$.
3. Use the exact shock relations from eq. (B.2) with the discontinuity located at $x_0 = -5\delta_0/2$.

First, the x–t diagram of density is presented in fig. B.14 for initializations 1 and 2 applied to configuration 1. When the shock-tube relations are used, a contact wave is also created at the initialization and interacts with the wave pattern before the end of the time frame of interest. This should not occur in the experimental setup as the shock tube is long enough to isolate the shock wave from the contact wave during the measurement time frame. This is why here, the exact shock relations are used instead to avoid this issue. If one would like to use the shock-tube relations, it would require a long numerical domain to reproduce the experimental setup, which is too expensive and unnecessary.

Then, the temporal evolution of the curtain width and edge positions are given in fig. B.15 for configuration 1. The initialization strategy impacts the spreading rate of the curtain. Even though initialization 1 is closer to the experimental results, it is not retained here because of the contact wave. Also the position of the shock from the exact shock relations does not modify the spreading rate. Indeed, the curves for initializations 2 and 3 superimpose in fig. B.15. From this observation, initialization 3 is preferred over initialization 2 as the physical time required for the shock to reach the curtain can be saved.

Appendix C. Mesh sensitivity

One of the most important parameters to assess the numerical setup is the mesh size. The mesh is built such that the number of cells in the curtain N_c is prescribed. Here, a mesh-independence study is performed with N_c ranging from 10 to 40. The curtain width, upstream edge and downstream edge evolution with time are plotted in fig. C.16. The curves for the highest refinement are close enough to consider that the results are independent of the mesh size with $N_c = 40$.

Appendix D. Particle diameter distribution

The particle diameter is expected to have some impact on the curtain width. Larger particles are expected to be slower as it has been shown in [18], and it is important to show to which extent this can impact the results. In reality, the diameter of the particles is in a range which can be quite large (above 10%), and it could be expected that a polydisperse particle curtain will show a larger width than monodisperse particles. This effect is detailed here by considering three diameters for configuration 2 of table 5: the minimum size $d_p = 106$ µm, maximum size $d_p = 115$

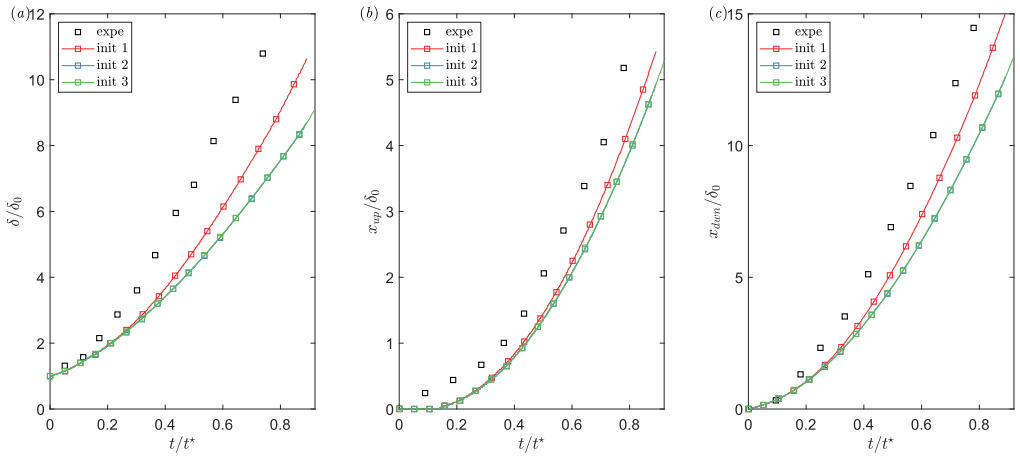

Figure B.15: Effect of initialization strategy on width (a), upstream edge (b) and downstream edge (c) evolution in time of the curtain for configuration 1. δ_0 is the initial curtain width and t^* is the characteristic time given by eq. (41). The blue and green curves are superimposed.

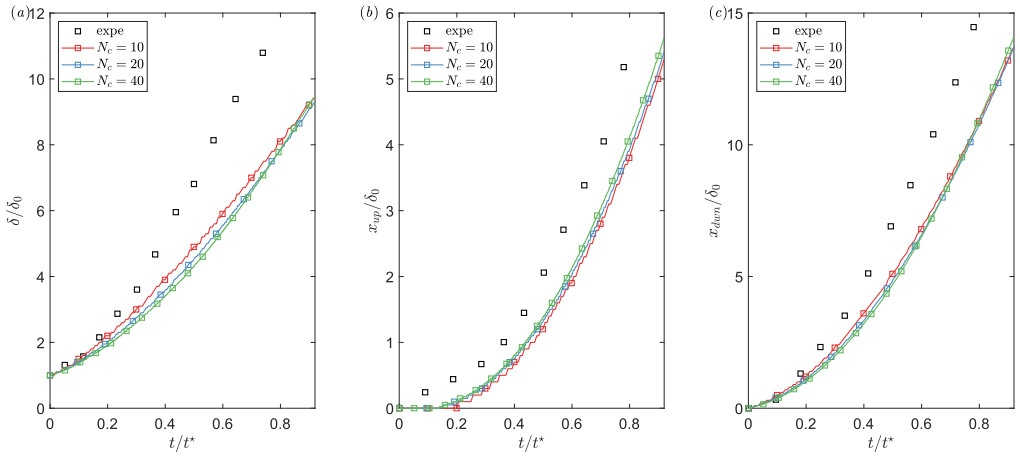

Figure C.16: Effect of mesh resolution on width (a), upstream edge (b) and downstream edge (c) evolution in time of the curtain. δ_0 is the initial curtain width and t^* is the characteristic time given by eq. (41).

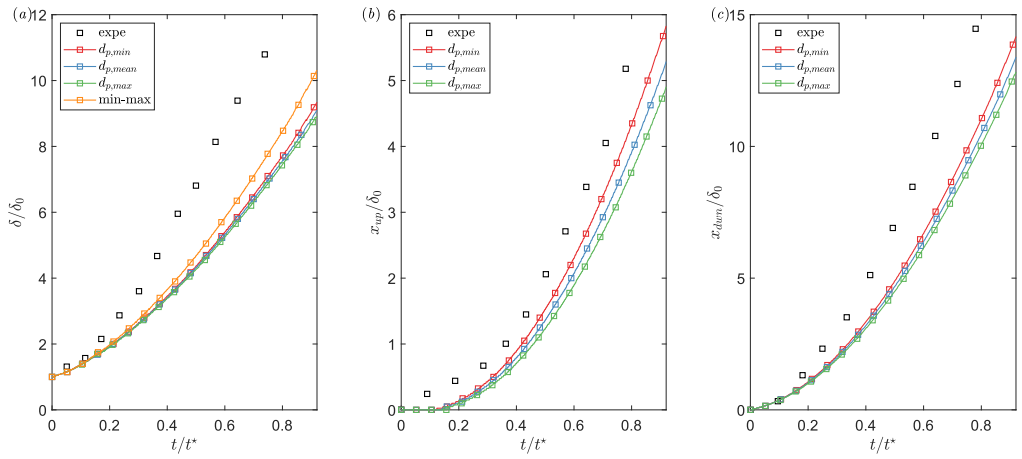

Figure D.17: Effect of particle diameter distribution on width (a), upstream edge (b) and downstream edge (c) evolution in time of the curtain. δ_0 is the initial curtain width and t^* is the characteristic time given by eq. (41). The "min-max" curve corresponds to the width computed from the upstream location of $d_{p,max}$ and the downstream location of $d_{p,min}$.

µm and mean size $d_p = 125$ µm. The curtain width, upstream edge and downstream edge evolution with time are plotted in fig. D.17 for the three diameters. As expected, large particles are stuck at the upstream edge and smaller particles are faster at the downstream edge. It is then expected that the resulting measured width in the experiment is larger than what can be simulated with a monodisperse model. To illustrate this, an additional curtain rate curve has been plotted by computing the width from the upstream location of $d_{p,max}$ and the downstream location of $d_{p,min}$. This last curve shows a larger spreading rate but still does not fit with the experimental data.